Modelling ruptures of buried high-pressure dense-phase CO_2 pipelines in carbon capture and storage applications - Part II. A full-scale rupture

Christopher J. Wareing[a,b,*], Michael Fairweather[a], Samuel A.E.G. Falle[c], Robert M. Woolley[a]

[a] *School of Chemical and Process Engineering, University of Leeds, Leeds LS2 9JT, UK.*
[b] *School of Physics and Astronomy, University of Leeds, Leeds LS2 9JT, UK.*
[c] *School of Mathematics, University of Leeds, Leeds LS2 9JT, UK.*

Abstract

Carbon capture and storage (CCS) presents a short-term option for significantly reducing the amount of carbon dioxide (CO_2) released into the atmosphere. National Grid initiated the COOLTRANS research programme to consider the CCS pipeline transportation of high-pressure dense-phase CO_2, including the development and application of a mathematical model for predicting the sonic near-field dispersion of pure CO_2 following pipeline venting or failure. In Part I (Wareing et al. IJGGC 2015 doi:10.1016/j.ijggc.2015.01.020) validation of this numerical model against experimental data was considered, with reasonably good agreement quantitatively and qualitatively demonstrated for a rupture of a 0.15 m external diameter pipeline. In this second part, the model is applied to the rupture of a 96 km pipeline with a nominal 0.61 m external diameter, the same as that proposed in the Don Valley CCS

*Corresponding author. Tel: +44 113 343 3871. Fax: +44 113 343 5090
Email address: `C.J.Wareing@leeds.ac.uk` (Christopher J. Wareing)
URL: `http://www.maths.leeds.ac.uk/~cjw` (Christopher J. Wareing)

Preprint submitted to International Journal of Greenhouse Gas Control August 20, 2015

Project. In the base-case, six snapshots of the flow dispersing into dry air are numerically simulated. Integrated mass and momentum fluxes exiting the crater are calculated, with the intention that they can be directly employed as source conditions for far-field dispersion simulations. The amount of solid CO_2 deposited in the crater is estimated through particle tracking techniques and six sensitivity studies vary crater properties.

The Don Valley CCS Project is co-financed by the European Union's European Energy Programme for Recovery.
The sole responsibility of this publication lies with the authors.
The European Union is not responsible for any use that may be made of the information contained herein.

1. Introduction

Carbon capture and storage (CCS) refers to a set of technologies designed to reduce carbon dioxide (CO_2) emissions from large industrial point sources of emission, such as coal-fired power stations, in order to mitigate greenhouse gas production. The technology involves capturing CO_2 and then storing it in a reservoir, instead of allowing its release to the atmosphere, where it contributes to climate change. Once captured, the CO_2 is transported and stored, typically underground, or used for processes such as enhanced oil recovery.

National Grid initiated the TRANSportation of Liquid CO_2 research programme (COOLTRANS) (Cooper, 2012) in order to address knowledge gaps relating to the safe design and operation of onshore pipelines for transporting dense-phase CO_2 from industrial emitters in the UK to storage sites offshore. This includes developing the capability for modelling the low-probability, high-impact worst case - an accidental release from a buried pipeline that contains CO_2 in the dense-phase. Learning from these studies can subsequently be combined with a range of other information to develop an appropriate quantified risk assessment (QRA) for a dense-phase CO_2 pipeline. With regard to modelling the worst case, the programme includes theoretical studies by University College London (UCL), the University of Leeds and the University of Warwick, carried out in parallel to provide "state of the art" numerical models for the pipeline outflow (UCL), near-field dispersion behaviour (University of Leeds) and far-field dispersion (University of Warwick) behaviour associated with below-ground CO_2 pipelines that are ruptured or punctured. Experimental work and studies using currently available practical models for risk assessment are being carried out by DNV GL (Allason et al., 2012).

The University of Leeds mathematical model (Wareing et al., 2013a) has been previously validated for free releases into air (Woolley et al., 2013; Wareing et al., 2014a), small-scale laboratory releases and dry ice particle behaviour (Wareing et al., 2013b, 2015b) and punctures of buried pipelines (Wareing et al., 2014b). In Wareing et al. (2015a) (hereafter referred to as Part I), the model was applied to a rupture experiment involving a 0.15 m external diameter pipeline - nominally 1/4 of the scale of the 'full-scale' 0.61 m external diameter pipeline proposed in the Don Valley CCS Project (Cooper, 2012; Cooper and Barnett, 2014). Numerical simulations were compared to experimental data, specifically measurements of temperature on a plane 1 m above the crater into which the release flowed. The comparison demonstrated reasonably good quantitative and qualitative agreement regarding temperatures and structures in the dispersion flow. Inconsistencies were interpreted as effects of differences between the ideal numerical initial condition and the real conditions in the experiment, only revealed through post-experiment investigations. Specifically the data-blind simulation assumed the two flows into the symmetric crater were identical. Investigations revealed this was not the case. Full details can be found in Part I. Here, in Part II, we consider the near-field flow in a full bore rupture of a buried full-scale pipeline. We define the near-field in this scenario as the region of the flow containing the sonic multi-phase shock-containing expansion regions around any pipeline rupture locations and interactions of flows in any crater formed by the rupture. The aim of this work is to produce validated flows at the termination of the near-field region, ideally at the top of the crater (ground-level), that can act as a thermodynamically accurate source condition for far-field modelling, defined as the regions of the flow outside and downstream of the near-field. The objective of this paper is to present these validated flows for far-field use. Previous modelling of the near- and far-field, discussed in detail in Part I, has lacked such sonic flow and thermodynamic accuracy. Consequent far-field dispersion in the COOLTRANS project has been modelled by the University of Warwick and is not in the scope of this paper.

The rupture is modelled as a break at the mid-point along a 96 kilometre (km) length of below-ground transportation pipeline. The rupture break is modelled as if an entire 12 m section of the pipeline has unzipped along the pipeline direction, then unrolled across the pipeline direction and separated from the rest of the pipeline, forming the base of crater and leaving two clean guillotine breaks in the pipeline at the locations where this section previously joined to the rest of the pipeline. This creates two identically-shaped inlets into the crater, each a cross-section of the pipeline. One is on the upstream side of the rupture, henceforth referred to as the upstream inlet, and one is on the downstream side of the rupture, henceforth referred to as the downstream inlet. This is commonly known as a ‘double-ended guillotine break’ in a pipeline. UCL have numerically modelled the pipe flow assuming instant removal of the section described above and provided a two-hour outflow prediction detailing the upstream and downstream inlet conditions. We use this prediction to define conditions at the upstream and downstream pipe inlets into the crater. Since it has not been computationally possible to simulate the entire outflow in sufficient detail to accurately capture the near-field thermodynamics, a method of simulating a number of instants in time, or snapshots of the sequence of steady-states that the flow passes through, with sufficient resolution has been used to investigate the rupture flow. Integrated mass and momentum flux through a horizontal plane at or above the crater (depending on the near-field flow structure) has been calculated for each snapshot. The size and shape of the crater remains constant, based on craters observed in experimental studies, the details of which were provided from DNV GL through the COOLTRANS research programme. To test the effect of different crater sizes and shapes on the dispersion flow through the crater, a number of sensitivity studies are performed.

We reviewed relevant CO_2 dispersion work previously and refer the reader to our recent publications in this area, specifically to Part I, to Wareing et al. (2014a) and to Wareing et al. (2014b). The work herein represents the first application of an accurate near-field model to an accidental rupture scenario involving a time-dependent decompression from a full-scale buried CCS pipeline. Other recent work in this area has been limited to above-ground free venting releases, or has used a similar near-field model to that described herein, but considered a constant crater source condition for the far-field modelling (Woolley et al., 2014).

In the next Section we review our mathematical model and numerical method. In Section 3 we present our methodology, including numerical techniques, initial conditions, sensitivity studies and particle tracking methods. The base-case numerical predictions are presented in Section 4 with the results of the sensitivity study presented in Section 5. Finally, the limits of applicability of these simulations are discussed in Section 6, followed by the conclusions and possibilities for future developments and improvements in Section 7.

2. Mathematical model and numerical method

The numerical approach is essentially the same as that adopted and validated in our earlier papers, discussed in detail in Part I. We reproduce the necessary details below.

2.1. Reynolds-averaged Navier-Stokes model

The Reynolds-averaged Navier-Stokes (RANS) equations, closed with a compressibility-corrected k-ϵ turbulence model, employed in this work are:

$$\frac{\partial \rho}{\partial t} + \nabla \cdot (\rho \mathbf{u}) = 0 \tag{1}$$

$$\frac{\partial \rho C}{\partial t} + \nabla \cdot (\rho C \mathbf{u}) - \nabla \cdot (\mu_T \nabla C) = 0 \tag{2}$$

$$\frac{\partial \rho \mathbf{u}}{\partial t} + \nabla \cdot (\rho \mathbf{u}\mathbf{u}) + \nabla P - \nabla \cdot \tau = 0 \tag{3}$$

$$\frac{\partial E}{\partial t} + \nabla \cdot [(E + P)\mathbf{u} - \mathbf{u} \cdot \tau] - \nabla \cdot (\mu_T T \nabla S) = 0 \tag{4}$$

$$\frac{\partial \rho k}{\partial t} + \nabla \cdot (\rho k \mathbf{u}) - \nabla \cdot (\mu_T \nabla k) = s_k \tag{5}$$

$$\frac{\partial \rho \epsilon}{\partial t} + \nabla \cdot (\rho \epsilon \mathbf{u}) - \nabla \cdot (\mu_\epsilon \nabla \epsilon) = s_\epsilon \tag{6}$$

where the variables have their usual meanings and are defined in the Notation section, noting that the vector velocity is expressed in bold as $\mathbf{u}$ and S is the entropy per unit mass. The turbulent diffusion coefficients are

$$\mu_T = \rho C_\mu \frac{k^2}{\epsilon}, \tag{7}$$

and

$$\mu_\epsilon = \frac{\mu_T}{1.3}, \tag{8}$$

with $\mathrm{C}_\mu = 0.09$. The turbulence production term is

$$P_t = \mu_T \left[\frac{\partial u_i}{\partial x_j} \left(\frac{\partial u_i}{\partial x_j} + \frac{\partial u_j}{\partial x_i} \right) \right] - \frac{2}{3} \nabla \cdot \mathbf{u} (\rho k + \mu_T \nabla \cdot \mathbf{u}), \tag{9}$$

where the summation convention has been assumed. The k source term is

$$s_k = P_t - \rho \epsilon \tag{10}$$

whilst the ϵ source term is

$$s_\epsilon = \frac{\epsilon}{k} (C_1 P_t - C_2 \rho \epsilon) \tag{11}$$

with $\mathrm{C}_1 = 1.4$ and $\mathrm{C}_2 = 1.94$. The turbulent stress tensor, τ, is

$$\tau_{ij} = \mu_T \left(\frac{\partial u_i}{\partial x_j} + \frac{\partial u_j}{\partial x_i} \right) - \frac{2}{3} \delta_{ij} (\mu_T \nabla \cdot \mathbf{u} + \rho k). \tag{12}$$

The k-ϵ turbulence model described here is coupled to a compressibility dissipation rate correction proposed by Sarkar et al. (1991). Comparisons of model predictions with this correction and experimental data have shown significant improvements over results derived using the standard k-ϵ approach for moderately and highly under-expanded jets of the type under consideration here (Cumber et al., 1994, 1995).

2.2. Equation of state

For CO_2, the composite equation of state described in Wareing et al. (2013a) is employed. This composite method predicts the thermophysical properties of the three phases of CO_2 for the range of temperatures of relevance to CO_2 dispersion from releases at sonic velocities, of interest to the CCS industry. This equation of state has been developed in such a way that is convenient for computational fluid dynamic applications; the gas phase is computed from the Peng-Robinson equation of state (Peng and Robinson, 1976), and the liquid and condensed phases from tabulated data generated with the Span & Wagner equation of state (Span and Wagner, 1996) and the DIPPR® Project 801 database (http://www.aiche.org/dippr/), academic access to which can be gained through the Knovel library (http://why.knovel.com). Pressure, gas and condensed phase densities, sound speed and internal energy have all been tabulated against temperature on the saturation line between 100K and the critical temperature, providing the basis for a fully functional form for differentiation, interpolation and extrapolation in numerical simulations. Air is modelled via an ideal gas equation of state with $\gamma_a = 7/5$.

2.3. Homogeneous equilibrium model

In previous work considering dense-phase CO_2 releases from small nozzles and punctures (Wareing et al., 2014a,b), particles of solid CO_2 do not reach equilibrium with the CO_2 gas flow in the initial expansion due to the short distance between release point and Mach shock when compared to particle thermal and dynamic relaxation times and velocities (Wareing et al., 2013b). There a relaxation model was applied to the movement of the condensed phase. In this work, where the distance between the release point and Mach shock is an order of magnitude or more times greater than the relaxation distances (dictated by the particle velocities and thermal and dynamic relaxation times (Wareing et al., 2013b, 2015b)) we assume that the condensed phase is in equilibrium with the vapour phase and no relaxation model is used.

2.4. Implementation

The composite equation of state is implemented within this homogeneous equilibrium model into MG, an adaptive mesh refinement (AMR) RANS hydrodynamic code (Falle, 1991). The code employs an upwind, conservative shock-capturing scheme and is able to employ multiple processors through parallelisation with the message passing interface (MPI) library. Integration in time proceeds according to a second-order accurate Godunov method (Godunov, 1959). In this case, a Harten Lax van-Leer (van Leer, 1977; Harten et al., 1983) (HLL) Riemann solver was employed to aid the implementation of complex equations of state. The disadvantage of the HLL solver is that it is more diffusive for contact discontinuities; this is not important here since the contact discontinuities are in any case diffused by the artificial viscosity. The artificial viscosity is required to ensure shocks travel at the correct speed in all directions and is at a very low level, decreasing proportionally with increasing resolution.

2.5. Adaptive meshing strategy

The AMR method (Falle, 2005) employs an unstructured grid approach, requiring an order of magnitude less memory and giving an order of magnitude shorter computation times than structured grid AMR. The two coarsest levels (0 and 1) cover the whole computational domain; finer grids need not do so. Refinement or derefinement depends on a given tolerance. Where there are steep gradients of variable magnitudes such as at flow boundaries or discontinuities such as at the Mach disc, this automated meshing strategy allows the mesh to be more refined than in areas of the free stream in the surrounding fluid. Each layer is generated from its predecessor by doubling the number of computational cells in each spatial direction. This technique enables the generation of fine grids in regions of high spatial and temporal variation, and conversely, relatively coarse grids where the flow field is numerically smooth. Defragmentation of the AMR grid in hardware memory was performed at every time-step, gaining further speed improvements for negligible cost through reallocation of cells into consecutive memory locations. The simulations presented below employed 5 levels of AMR and hence a low level of artificial viscosity. A grid resolution control has been imposed in the AMR, allowing for the full resolution of the sonic decompression and Mach shock near the inlet pipes and also the larger scale of the crater, extending a few metres above and to the sides of the crater, in order to establish the flow out of the crater on a plane above the near-field of the release. This was required to achieve reasonable computational execution times (on average 100,000 CPU hours per run, more for higher resolution convergence tests).

3. Methodology

3.1. Quasi-steady-state flows

Quasi-steady-state flows were achieved by integrating the simulations until the flow out of the top of the crater did not change and the integrated mass-flux leaving the crater through a horizontal plane at or above ground-level matched the integrated mass-flux into the crater from the combined pipe inlets. These are henceforth referred to as 'steady-state' flows. Steady-state flows were typically achieved in a physical time of less than 1 second. They are convergent, tests with higher resolutions, a single symmetry and no symmetry boundaries having shown that the flow structure is qualitatively and quantitatively closely similar to the results presented here. It should also be noted that small variations in pressure, temperature and velocity at the inlets do not greatly affect the steady-state flow structure, shifting only the position and width of the Mach shock very slightly, with little to no effect on the post-shock flow conditions, although if these variations unbalance the inlet conditions between upstream and downstream pipes, large effects can be observed, moving the flow out of the crater away from the centre of the crater as shown later in this work.

3.2. Pipeline inlet conditions

The full-scale rupture modelled is a double ended guillotine break at the mid-point along a 96 km length of below-ground transportation pipeline, with external diameter (d) of 0.61 m and pipeline wall thickness of 19.4 mm. It is henceforth referred to as the 'base-case'. A single 12 m section of pipeline has ruptured, in effect unzipping, flattening and dropping to form the base of the crater as previously described. The pipeline has a 1.2 m depth of soil cover. Valves are located 8 km upstream and 8 km downstream of this break. Valve closure begins after 900 s and the valve closure time is 30 s. At the time of the break, the pipeline is assumed to be filled with stationary dense-phase CO_2 at an initial pressure at the upstream end of the pipeline of 150 barg and temperature of 303 K. We employ predictions of the pipeline outflow calculated by UCL and provided through the COOLTRANS research programme. This model has recently been applied to the modelling of CO_2 discharge following full-bore rupture of pipelines (Brown et al., 2013) where it was shown to produce reasonable agreement in comparison with available experimental data.

The inlet pressure at each pipe end predicted by UCL is shown in Figure 1. As can be seen from this figure, the variation of inlet pressure with time is slow compared to the thermal and dynamical relaxation times in this decompression, which are fractions of a second (Wareing et al., 2013b, 2015b). The variation of the other inlet conditions is also slow i.e. temperature, velocity, mass-flow and condensed phase fraction. The velocities in the near-field are high (greater than 50 $m\,s^{-1}$) with flow times across the crater and into the plume consequently short (less than 0.5 s). The decompression flow therefore passes through a sequence of steady states, as the steady-state flow out of the crater is achieved in typically less than a second, considerably faster than the variation of inlet conditions affects the near-field. Hence, as it not computationally possible to simulate the entirety of the decompression (due to hardware and time constraints), it is entirely reasonable to simulate a number of representative steady states, or 'snapshots', at specific times that

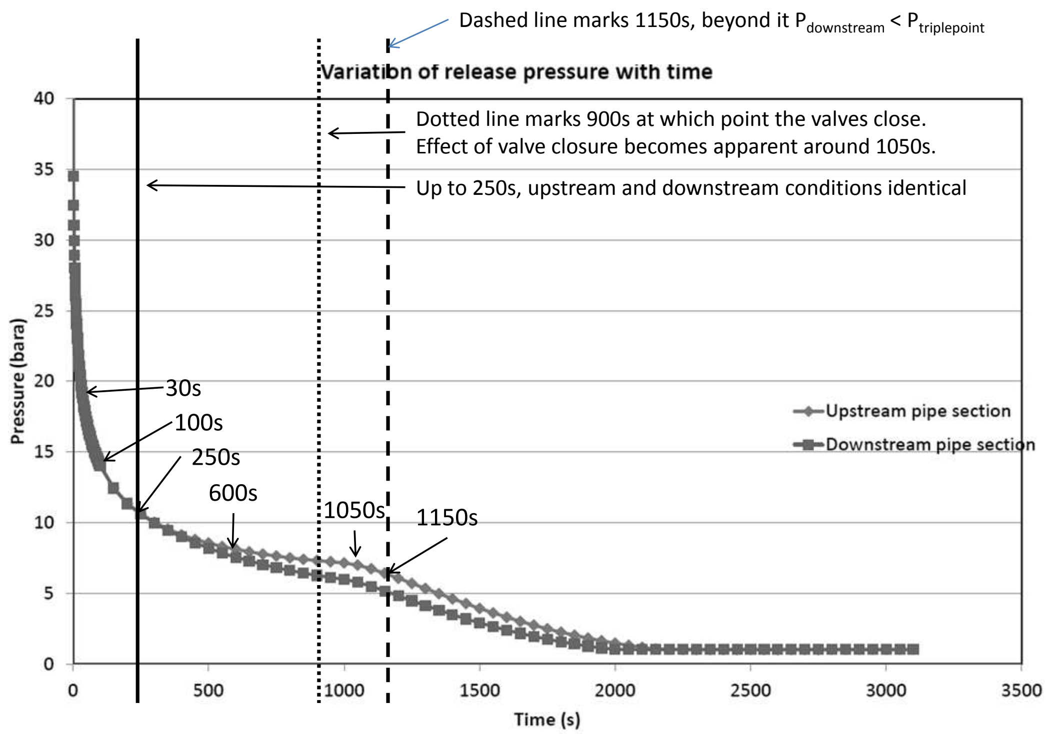

Figure 1: Prediction of the variation of the inflow pressure with time in the base case (Mahgerefteh, private communication) and the points chosen for snapshot simulations.

represent or bracket points of interest in the decompression, as is frequently done in performing such pipeline risk assessments. Further, enough snapshots had to be modelled such that a reconstructed extrapolated flux for the entire duration would represent the smooth variation of the flow, to be presented in a future publication. In discussion with DNV GL through the COOLTRANS research programme, these snapshots were specified at $t = 30$ s, 100 s, 250 s, 600 s, 1000 s and 1150 s for the base case. Complete prescriptions of the inlet boundary conditions at these times at the upstream and downstream pipe inlets into the crater are shown in Table 1. The snapshots at 30, 100 and 250 s cover the duration of the decompression where the upstream and downstream pipeline inlet conditions are identical - they are 'balanced'. Given the range of pressures (and hence saturated temperatures), these three snapshots were chosen to cover the initial high pressure, high mass-flow period. Although the pressures were higher earlier than 30 s, it was concluded that the first seconds of the rupture may be heavily affected by the clearance of overlying soil and the formation of the crater, so no earlier snapshots were computed. The snapshots at 1000s and 1150s were chosen in order to bracket the time at which the valve closure has an effect on the flow into the crater, shown in Figure 1. A final snapshot at 600 s was chosen in order to characterise the period of unbalanced flow (where the upstream and downstream inlet conditions differ) before the effect of the valve closure became apparent on the inlet conditions. Beyond 1150s, the downstream pipe inflow rate drops below the triple point. Given that the flow rates have decreased considerably compared to their initial values in the first 10 s of the rupture and questions arise over the multiphase flow behaviour below the triple point, we do not to model any snapshots beyond 1150 s at this time. The impact of these assumptions is discussed in Section 6.

3.3. Crater geometry

The geometry of the crater is illustrated in Figure 2. It is assumed that the crater is shaped like a 'bath tub', with a horizontal rectangular section at its base of length L' and width W'. The length of the flat section is assumed to be equal to the fracture length of a complete single section and its width is assumed to be equal to the circumference of the pipeline, centered on the original position of the pipeline, as if a section of the pipeline has

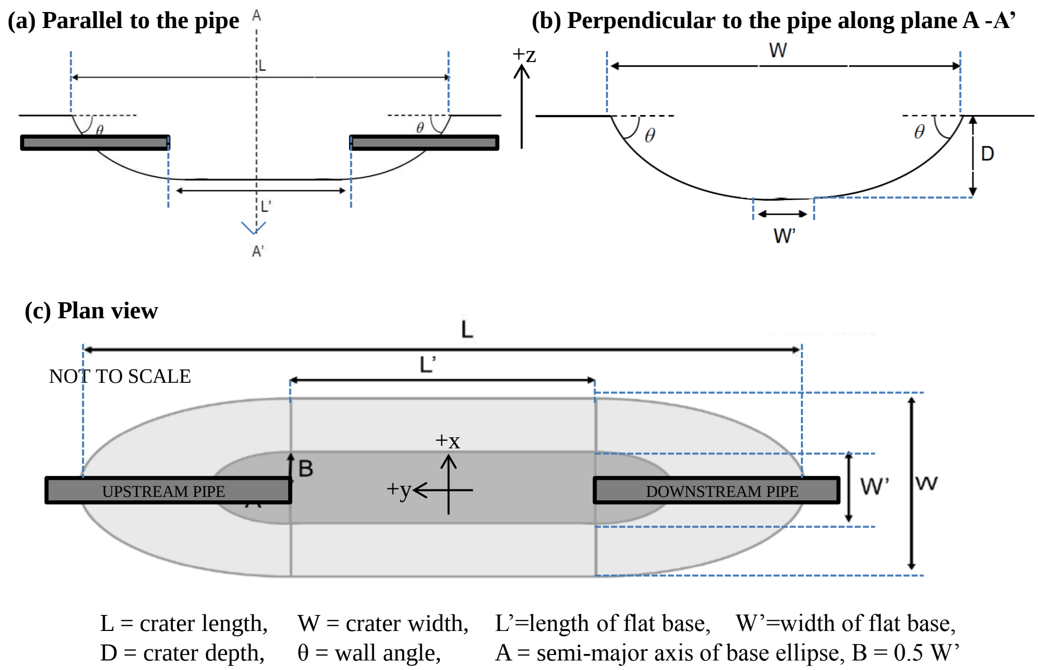

Figure 2: Details of the crater used in the full-scale rupture simulations (Cleaver, private communication).

unzipped and then unrolled, leaving the neighbouring sections in tact. The flat base is at the maximum crater depth, D. The dimensions of the crater have been estimated using the DNV GL COOLTRANS crater formation predictive model, based on real craters generated in incidents. The values that have been obtained are given in Table 2 for the base-case rupture As a first order modelling scenario, this represents the worst case failure of a pipeline reasonably well. Other failure scenarios will result in lower, less collimated, flow rates.

3.4. Numerical mesh and initial domain conditions

In computationally simulating this crater release, a three-dimensional Cartesian coordinate grid mesh has been employed. The inlet conditions at the upstream and downstream inlet pipes in the crater, as shown in Table 1, are enforced on every timestep of the simulation. The initial state of the fluid in the rest of the domain consists entirely of stationary air at atmospheric pressure and a temperature of 283 K. The surface of the crater has been defined using ellipses. The two ends of the flat base are flat ellipses. The method for joining the flat section of the crater to the crater rim in a smooth manner is based on ellipses calculated from the dimensions and wall angle of the crater, ensuring a smooth change of depth and a constant crater wall angle perpendicular to the pipeline at all positions along the rim. Below this 'surface', in the ground, no numerical integration is carried out and the ground is considered solid.

Symmetry boundaries were used where possible in these simulations. Specifically, as the inlet pipe flows are balanced for the 30 s, 100 s and 250 s snapshots as indicated by the overlapping upstream and downstream predictions in Figure 1, two symmetry boundaries were used in order to reduce the computational effort and achieve steady state with minimum execution time. The symmetry boundaries were imposed vertically at $x = 0$ m, parallel to the pipeline through the centre of the pipeline, and vertically at $y = 0$ m, perpendicular to the pipeline through the centre of the crater. A quarter crater was hence simulated on the domain (x, y, z) (0, 0, -3.5) m to (15, 10, 11.5) m. The single pipeline inlet is semi-circular in this domain and located on the x-z plane at $y = 6$ m, with the centre located at (0, 6, -1.2), with a radius of 0.3 m. A solid pipeline was modelled for $y > 6$ m. For the 600 s, 1000 s and 1150 s snapshots, where the upstream and downstream predictions do not overlap in Figure 1, only a single symmetry boundary was used as the inlet pipe flows are unbalanced, specifically at the $x = 0$ m boundary parallel to the pipeline and through its centre. A half crater was hence simulated on the domain (x, y, z) (0, -10, -3.5) m to (15, 10, 11.5) m. The upstream and downstream pipeline inlets are semi-circular in this domain and located on x-z planes at constant y. The upstream inlet is at $y = 6$ m with the centre of circle located at (0, 6, -1.2), and a radius in x-z plane of 0.3 m. The downstream inlet is at $y = -6$ m with the centre located at (0, -6, -1.2), and a radius in x-z plane of 0.3 m. Solid pipelines were modelled for $y > 6$ m and $y < -6$ m. The remaining boundaries were set to free-flow, only allowing the in-flow of air with the initial atmospheric condition when in-flow was detected e.g. air dragged in from behind the pipe inlets. In all cases, the coarsest grid cell size (on AMR level 0) was $0.5 \times 0.5 \times 0.5$ m. The finest grid cell size (on the AMR level 4) was $3.125\times\ 10^{-2}$ m on a side. This is equivalent to a fixed grid resolution of $480 \times 480 \times 320$ cells for the quarter crater simulations and equivalent to a fixed grid resolution of $480 \times 480 \times 640$ cells for the half crater simulations.

As symmetry axes were used, cross-winds were not modelled in the cases presented here. Four test simulations were performed to establish the validity of this approach, considering a quarter-crater (with two symmetry axes), a half-crater (with one symmetry axis along the pipeline), a full crater (with no symmetries) but with still air and finally a full crater with a cross-wind of 2 $\mathrm{m\,s^{-1}}$. A comparison of the results showed that at the crater rim or just above it, the flow out of the crater is fast enough (on the order of 100 $\mathrm{m\,s^{-1}}$) not to be affected by the cross-wind and hence it has been ignored in these near-field simulations. Further, the possibility of reentrainment of a cooled CO_2 and air mixture, rather than just ambient air, has not been considered, as to do this accurately would require a coupled near and far-field computation, beyond the immediate capability of this model. These assumptions and limitations are discussed in the penultimate section of this article, Section 6.

3.5. Sensitivity studies

The sensitivity studies consider variations of crater size and shape only, keeping the pipe inlet conditions the same as in the base-case rupture. Details of the sensitivity study variations are specified in Table 2. Numerical domains were extended by increasing numbers of cells as necessitated by the variation of crater size, but the base resolution as above was kept constant. A single snapshot (at $t = 250$ s) is simulated for each study, unless unexpected behaviour or features become apparent, or there is specific industrial interest in the case, detailed later.

3.6. Integrated fluxes

During establishment of a steady-state flow in the near-field, fluxes are monitored through a horizontal plane in the simulation, either at or just above ground level depending on how far the shock expansion zone protrudes out of the crater above ground level. The CO_2 mass flow, or flux, into the simulation domain from the upstream and downstream pipeline inlets is defined in the initial condition and it is to this total input CO_2 mass flux that the CO_2 mass flux through the plane is compared. The mass flux is calculated by integration of the mass flowing through this plane, for the total mass, CO_2 mass and solid CO_2 mass. Momentum flux is calculated by a similar integration for the total momentum, CO_2 momentum and solid CO_2 momentum. Simple velocities are inferred by dividing the integrated momentum by the integrated mass.

3.7. Particle deposition

In order to estimate particle deposition in the crater, a Lagrangian particle tracking method has been one-way coupled to the fluid-flow model and used to inject and track the movement of particles through the crater. This method has been proved successful in modelling particle behaviour in below-ground pipeline puncture modelling (Wareing et al., 2014b) and also in small-scale laboratory releases (Wareing et al., 2013b, 2015b). As this previous work has shown that the CO_2 particles are in equilibrium with the flow for large-scale releases they are injected in the inlet region with the same initial velocity vector magnitude and direction as the CO_2 fluid. They have a radius of 2×10^{-6} m and are given a density appropriate to solid phase CO_2 at the sublimation temperature, based on properties measured in our recent laboratory scale experiments (Wareing et al., 2013b). The movement of the particles is then computed, including drag effects, through a one-way coupling where the fluid influences the particles and not vice versa, until the particles begin to leave the simulation domain. Any particles that have hit the crater walls and stuck there are assumed to have been deposited in the crater and counted. This number is converted to a percentage of the original number of particles inserted into the flow and then scaled to the solid mass flux into the crater post Mach shock in order to obtain a rate of solid CO_2 mass deposition into the crater.

4. Numerical results for the base-case rupture

In this section, Figures 3 to 9 are either shown on vertical or horizontal planes through the numerical domain. Specifically, the vertical y-z plane is always through the centre of the crater at the midpoint of the pipeline rupture, parallel to the initial velocity vectors and the $x = 0$ m boundary. The position of the horizontal x-y plane varies in z from $z = 0$ m (ground-level) to $z = 2$ m. Each figure shows (a) temperature, (b) CO_2 fraction, (c) solid CO_2 fraction, (d) velocity and (e) density.

4.1. Simulated flow 30 seconds after rupture

Figure 3 shows the predicted steady state flow on the vertical plane at $t = 30$ s. The expansion zone as the CO_2 exits the pipeline is clearly visible in temperature, velocity and density. In this region, the lowest temperatures are reached, passing below the triple point and freezing the remaining liquid CO_2 into the solid phase. Just before the Mach shock at the termination of this zone, the highest velocities and lowest pressures are reached. Beyond the Mach shock, the temperature is at the sublimation temperature as both solid and gas phase CO_2 are present, enforced by the homogeneous equilibrium model for pure CO_2. The overall fluid (CO_2 and air) temperature drops slowly as air is mixed into the jet and the plume exits the crater. The solid fraction just beyond the Mach shock is around 0.35 and this only begins to drop outside the crater, indicating sublimation only begins to occur as the jet leaves the crater. The core and sheath nature of the sonic jet is clear

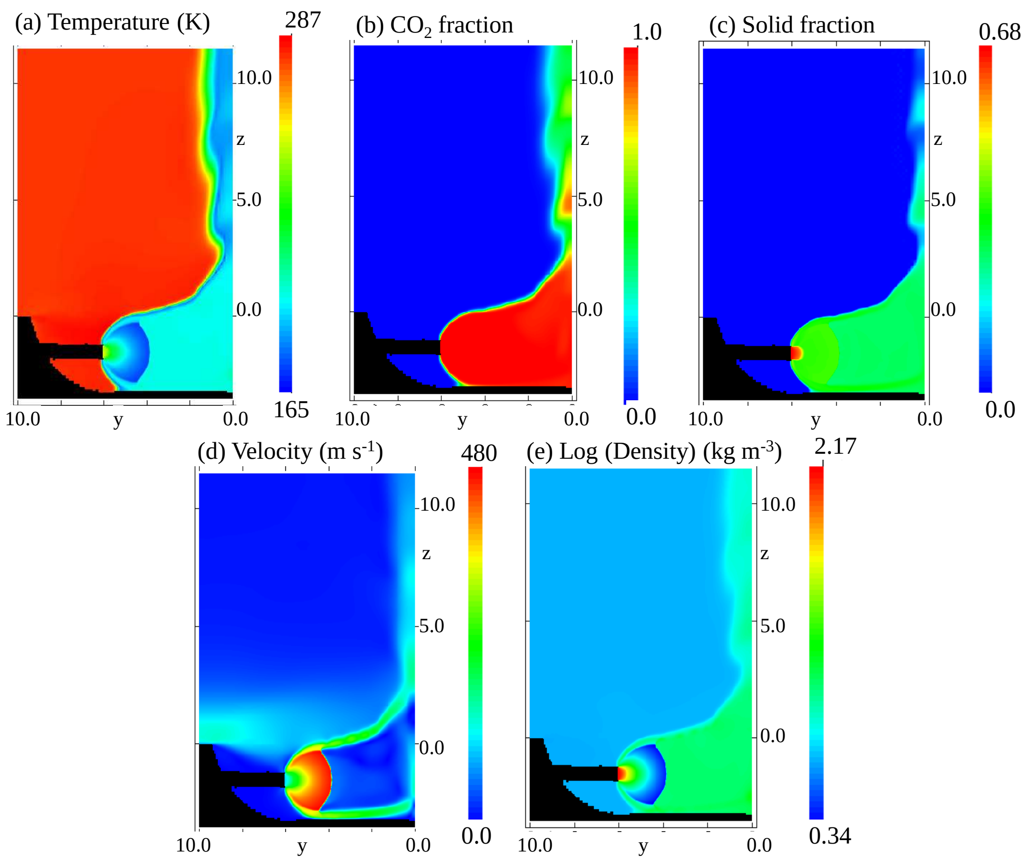

Figure 3: Vertical plane through the crater at t=30 s.

in the plot of velocity, where the vertical slice shows the slow moving core surrounded by the fast moving sheath. On interaction with the oncoming jet at the $y = 0$ m symmetry boundary, the flow is diverted upwards, but also spreads out perpendicular to the pipeline axis. This spreading lateral flow then runs up the crater walls and leaves the crater inclined at the crater wall angle. The velocity plot shows that as expected air is entrained into the crater from behind the pipeline inlets at a rate of a few tens of metres per second.

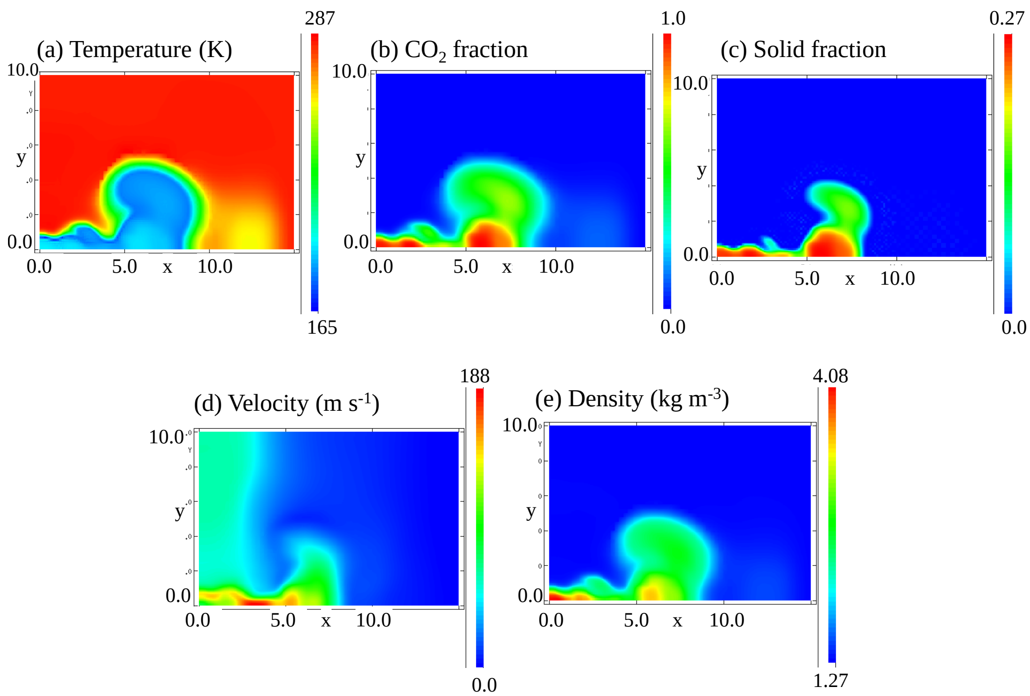

Figure 4: Horizontal plane 2 m above the crater at t=30 s.

Figure 4 shows the flow on the horizontal plane 2m above the crater. This is the lowest height at which the horizontal plane does not intersect the near-field expansion zone terminated by the Mach shock and the associated high-velocity jet structure and hence is the lowest plane at which data can be passed to a far-field simulation. The highest densities and CO_2 fractions are in a jet directed upwards in the centre of the crater (at the origin (0,0) of the numerical grid) and in the lateral spread of the flow turned upwards by interaction with the crater at $x = 5$ m to $x = 7$ m on the x axis. The peak velocities are between these two regions, but this region is less dense and hence carries less momentum. The jet still contains up to approximately 25% solid CO_2 at this height and hence the temperature in this equilibrium model is below the sublimation temperature in CO_2 and air mixture. Whilst the peak velocity is up to 188 $\mathrm{m\,s^{-1}}$, the average velocity is less than half this. Integrated mass and momentum fluxes on this plane are shown in Table 3.

4.2. Simulated flow 100 seconds after rupture

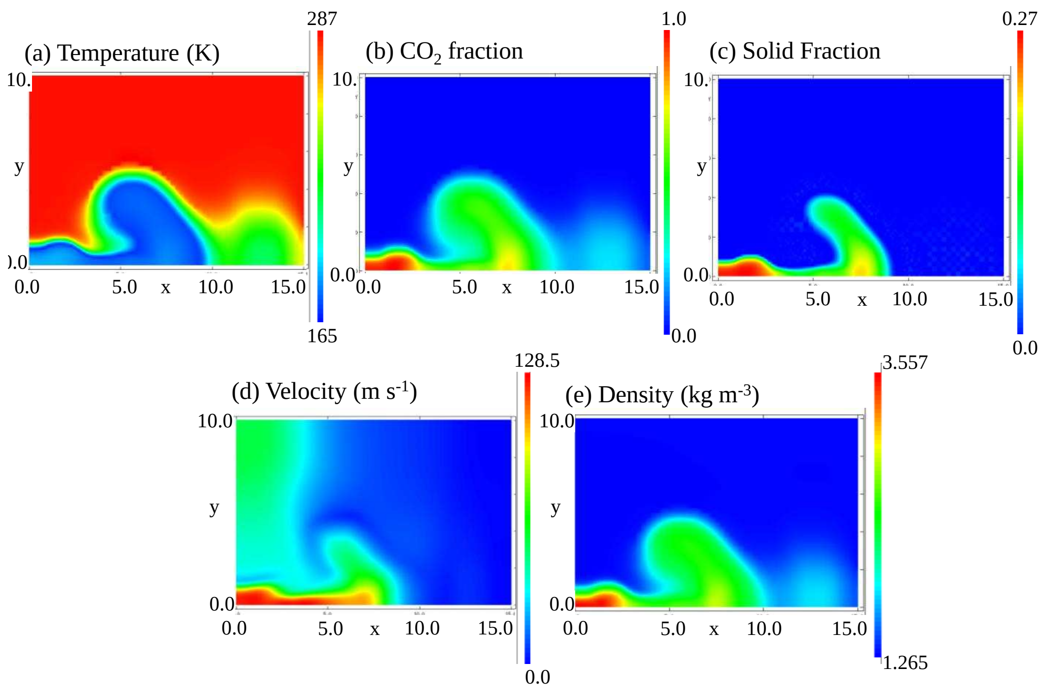

Figure 5: Horizontal plane 2 m above the crater at t=100 s.

In this case, the expansion zone is smaller (as the pressure at the pipe inlet is lower). Compared to the steady-state flow at $t = 30$ s, the structure is somewhat smoother and more collimated into a fan shape out of the centre of the crater perpendicular to the pipeline. Figure 5 shows the flow on a horizontal plane 2m above the crater. Even though the inlet pressure is lower, this is still the lowest height at which the horizontal plane does not intersect the near-field expansion zone terminated by the Mach shock and associated high-velocity jet structure, and hence is the lowest plane at which data can be passed to a far-field simulation. The highest densities, CO_2 fractions and highest velocities are in the fan perpendicular to the pipeline directed upwards in the centre of the crater (at the origin (0,0,0) of the numerical grid), laterally spreading along the x axis. The cloud expanding towards positive y away from the x-axis in Figure 5 at around $x = 7.5$ is a result of the flow from the interacting jets in the centre of the crater running up the crater wall below this plane and then spreading upwards and backwards toward the pipeline. The integrated upwards mass and momentum fluxes on this plane are shown in Table 3.

4.3. Simulated flow 250 seconds after rupture

The expansion zone is smaller than at $t = 100$ s due to the lower inlet pressure. Compared to the flow at $t = 100$ s, the width of the jet in the crater and the resulting upwards plume are smaller and carrying less CO_2, although the solid fraction is still the same. The velocities in the jet are on an identical range to those noted in the earlier base-case rupture snapshots. The expansion zone at the end of the pipe is now almost entirely below the ground level. The structure of the flow on a plane 1m above the crater, as this is now the lowest plane that can be considered without interference from the near-field expansion zone, is quantitatively and qualitatively similar to that at $t = 100$ s. The highest densities and CO_2 fractions are now in an oval cold plume moving directly upwards (toward positive z) form the centre of the crater at around at 80 to 100 $\mathrm{m\,s^{-1}}$. The integrated upwards mass and momentum fluxes on this plane are shown in Table 3.

4.4. Simulated flow 600 seconds after rupture

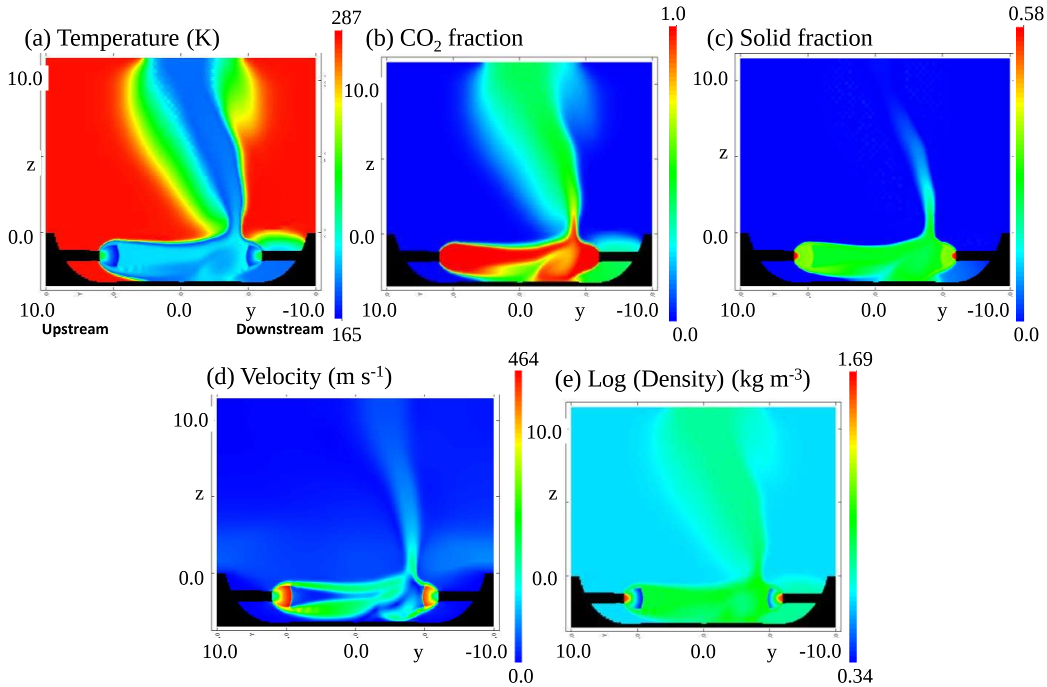

Figure 6: Vertical plane through the crater at t=600 s.

Figure 6 shows the predicted steady state flow at $t = 600$ s on the vertical slice described previously. The flows out of the pipes into the crater are now unbalanced i.e. the upstream and downstream inlet conditions are different and the predictions no longer overlap in Figure 1. The higher pressure of the upstream inlet flow has pushed the exit plume over toward the lower pressure downstream inflow. Compared to previous snapshots, as expected with lower inlet pressures, the expansion zones are now smaller. The fraction of CO_2 in the solid phase is still the same at the crater rim.

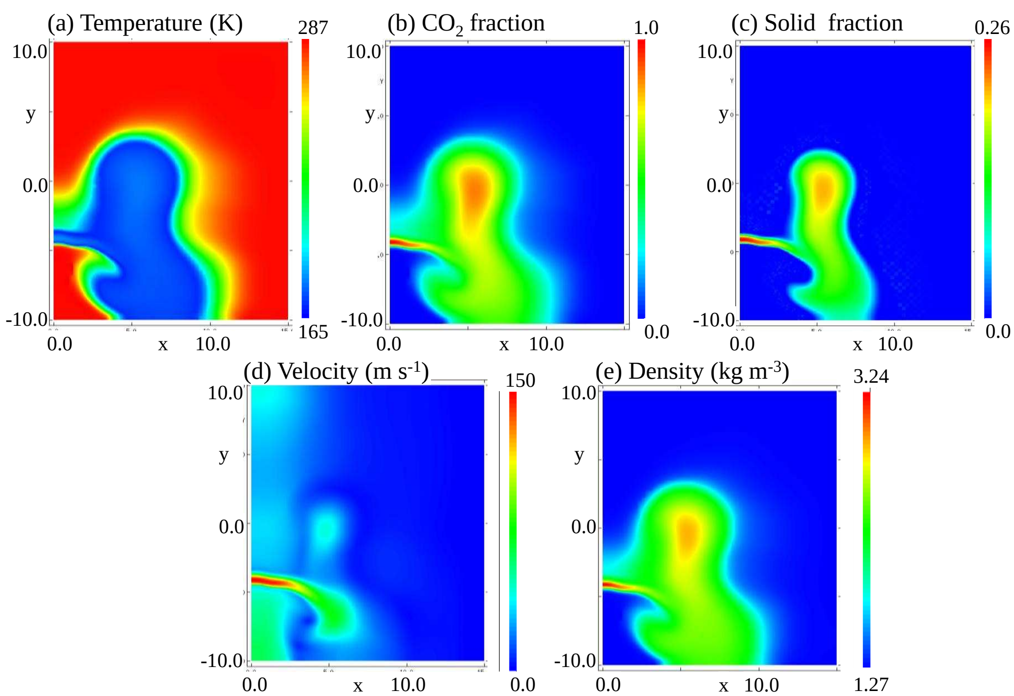

Figure 7: Horizontal plane 1 m above the crater at t=600 s.

Figure 7 shows the flow on a horizontal plane 1m above the crater. This is the lowest height at which the horizontal plane does not intersect the near-field expansion zone terminated by the Mach shock and associated high-velocity jet structure and hence is the lowest plane at which data can be passed to a far-field simulation. The flow out of the crater is in the form of a thin fan directed upwards from the interaction region, which in this steady-state snapshot is moved from the centre of the crater toward the downstream pipe. Compared to previous snapshots with balanced inlets, the flow out of the crater is still narrow in the centre of the crater above the pipeline axis, but widened by the crater walls and unbalanced inlets toward positive x. It should be noted that this simulation, with only one plane of symmetry at

$x = 0$ m, shows the same fan jet structure emerging from the crater as the previous three snapshots, albeit shifted toward the downstream pipe. The integrated upwards mass and momentum fluxes on this plane are shown in Table 3.

4.5. Simulated flow 1000 seconds after rupture

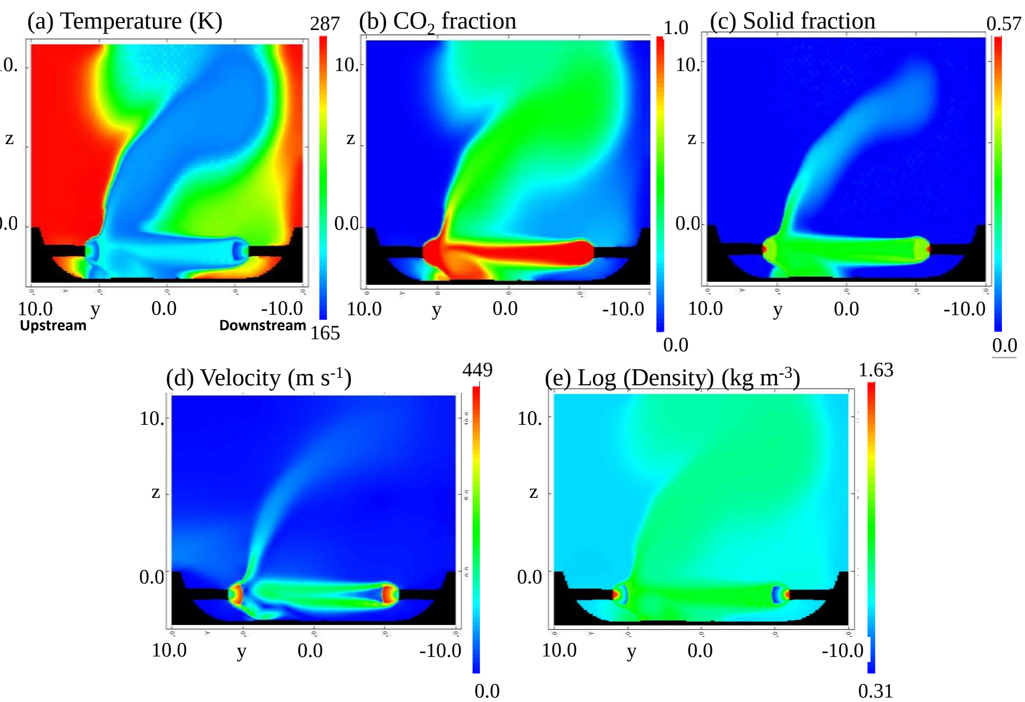

Figure 8: Vertical plane through the crater at t=1000 s.

Figure 8 shows the predicted steady state flow at $t = 1000$ s. The upstream and downstream pipe flows into the crater are unbalanced and the fan jet leaving the crater is now close to the upstream Mach shock. The velocity plot shows the downstream jet remains fairly collimated across the whole crater. The lower pressure at the downstream pipe inlet results in a smaller diameter Mach shock and a smaller jet diameter post-Mach-shock. It is apparent that the jet from the downstream inlet has been able to split the upstream jet. Whilst it is possible that this result is a numerical issue, this is unlikely given the behaviour observed in the sensitivity studies and at other times, where stable jets form and the location of the stagnation point is stable. It is also possible to speculate whether this effect should have shown up at earlier simulation times but for the use of symmetry planes. The cross-wind tests using quarter, half and full craters have shown no movement of the stagnation point. The simulation has also been advanced in time to examine whether the near-field has not yet reached structural steady-state. No shift away from the current position was observed. The CO_2 fraction is lower in the plume, rapidly dropping to 50% by a few metres above the crater, although the fraction of CO_2 in the solid phase is on the same order as all previous snapshots.

Figure 9 shows the flow on a horizontal plane 1m above the crater. This is the lowest height at which the horizontal plane does not intersect the near-field expansion zone terminated by the Mach shock and associated high-velocity jet structure and hence is the lowest plane at which data could be passed to a far-field simulation. The flow out of the crater is in the form of a thin fan directed upwards from the interaction region, which in this snapshot is moved toward the upstream pipe and bent toward the downstream pipe as a result of the air inflow into the crater behind that pipe which is forcing the upwards plume fan to bend over toward the downstream pipe. It is worth noting that the upwards flow is still vertical and unaffected by the air inflow for the first few metres. As the air is flowing into the crater at velocities

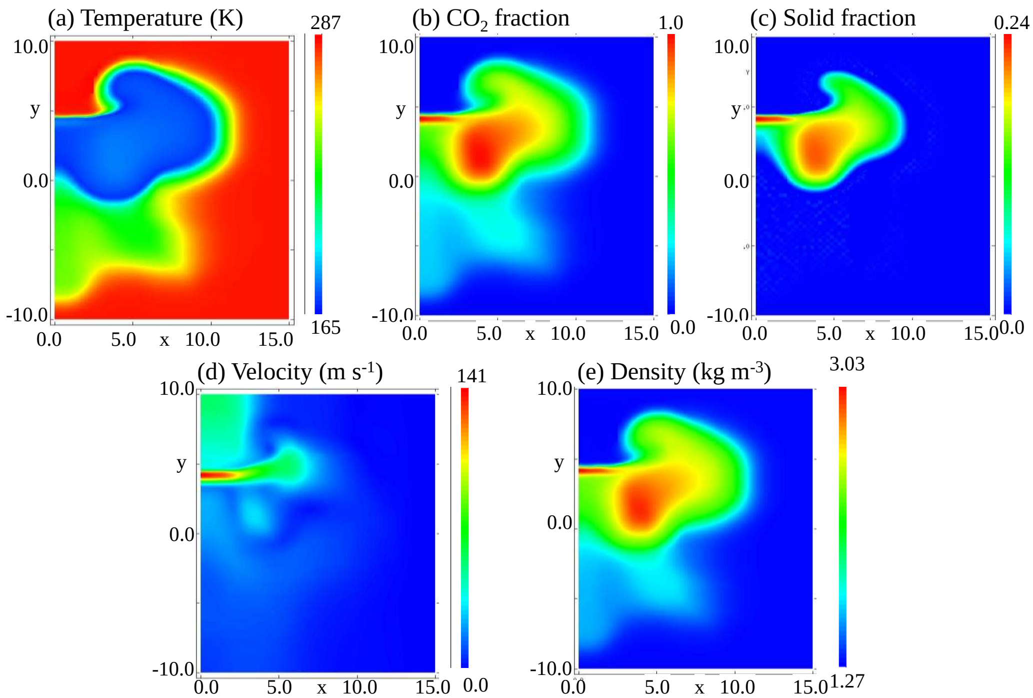

Figure 9: Horizontal plane 1 m above the crater at t=1000 s.

on the order of tens of metres per second, this further supports the previous tests that show cross-winds of a few metres per second do not affect the initial vertical flow out of the crater, and hence the use of symmetry planes is justified. The integrated mass and momentum fluxes on this plane are shown in Table 3.

4.6. Simulated flow 1150 seconds after rupture

The upstream and downstream inlet conditions remain unbalanced. As in the previous snapshot at $t = 1000$ s, the downstream jet has pushed the interaction region back to the Mach shock of the upstream crater inlet, with the upwards plume close to the upstream Mach shock. The balance is still towards the momentum of the downstream jet with a smaller cross-sectional area. The flow on a plane above the crater is very similar to that predicted at $t = 1000$ s, in the form of a thin fan directed upwards from the interaction region in the crater, with lateral spreading from material flowing up the crater wall. The integrated mass and momentum fluxes on this plane are shown in Table 3.

4.7. Particle deposition

Figure 10 shows the particle locations after the particles have been allowed to evolve through the flow until one or more have left the computational domain. In the first three snapshots (panels (a), (b) and (c)), at times when the flow from the upstream and downstream pipelines is balanced, we find no particles embed into the crater walls and hence no solid is deposited into the crater. At $t = 600$ s, 1.5% of the particles introduced have been deposited into the crater walls, primarily through the flow coming from downstream inlet pipe flow split by the upstream flow. At $t = 1000$ s, 1% of the particles introduced have been deflected into the base of the crater, this time near the upstream pipe rupture; the same occurs at $t = 1150$ s.

An important question in the quantified risk assessment of this rupture scenario is how much solid is deposited in the crater. We now consider two particle deposition scenarios. First, the more extreme case, where we average across the entire duration of the release and estimate that approximately 1% of particles released during a full-scale pipeline rupture end up embedded in the base of the crater. Based on this, a total of 14,000 kg of solid CO_2 could be deposited over the 1150s before the pressure at the downstream rupture reaches the triple point. This is equivalent to 10 cubic metres of solid CO_2 spread around the base of the crater. covering the base to a

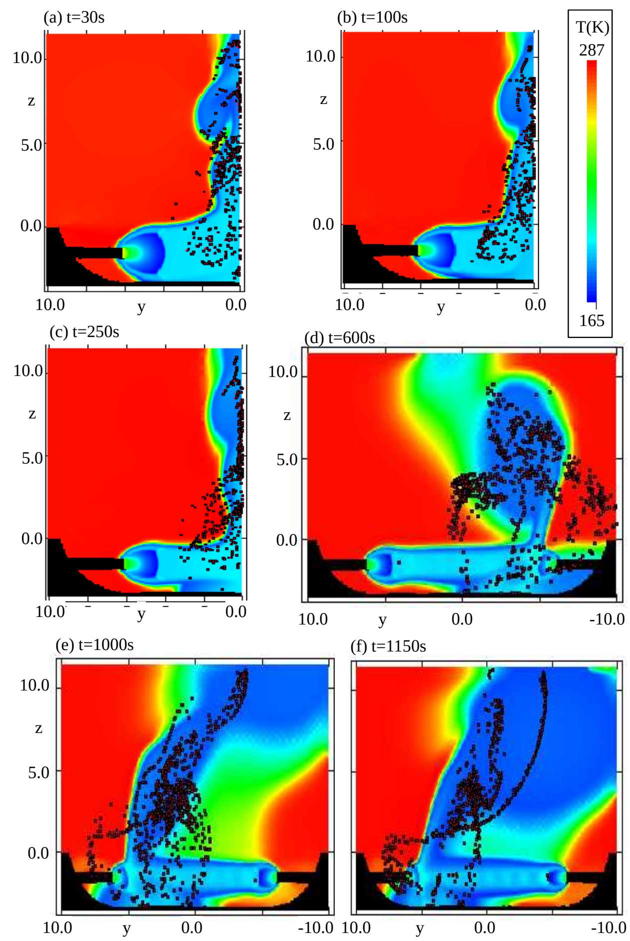

Figure 10: Vertical planes through each of the base-case snapshots with particles. Panels (a), (b) and (c) only show half the slice through the crater as they were quarter crater simulations. Onto each plane are collapsed all the locations of the particles in the entire three-dimensional simulation, marked by red squares. Particles considered to be deposited in the walls are shown as the red squares inside the black solid walls.

depth of approximately 0.4m. Secondly, we assume that whilst the pipeflows are balanced up to 250 s, there is no particle deposition in the crater. An integration from 250 s to 1150 s reveals that approximately 8500 kg of solid

CO_2 could be deposited in that time - 40% less than in the first scenario.

5. Sensitivity studies

For reference, details of the sensitivity studies are summarised in Table 2. Unless specifically detailed, the initial conditions were identical to the base case.

5.1. Sensitivity study 1 - a longer fracture

In the first sensitivity study (S1), the pipeline fracture length is doubled to 24m and the crater size changed according to Table 2. The motivation for this study is to examine the consequences of constructing the pipeline from 24 m sections, rather than 12 m in the base case. All six equivalent snapshots of the flow have been simulated in this case. The integrated upwards mass and momentum fluxes are presented in Table 4. The effect of changing fracture length appears to smooth and balance the flow from the centre of the crater, and leading to lower CO_2 and solid CO_2 fractions in the plume out of the crater. The effect on the flow out of the crater compared to the base case is due to the greater distance between the upstream and downstream pipes, which gives a greater distance before the two jets interact, which in turn results in a more collimated flow out of the crater.

As a result, the plume out of the crater has a very similar shape and position in the centre of the crater at all six times considered. The flow on a horizontal plane above the crater is shown in Figure 11(b). The upwards flow is very symmetric with a thin fan perpendicular to the pipeline in the centre of the crater at all times, with lateral spreading of the cloud caused by interaction with the crater wall as the flow moves outward from the pipeline

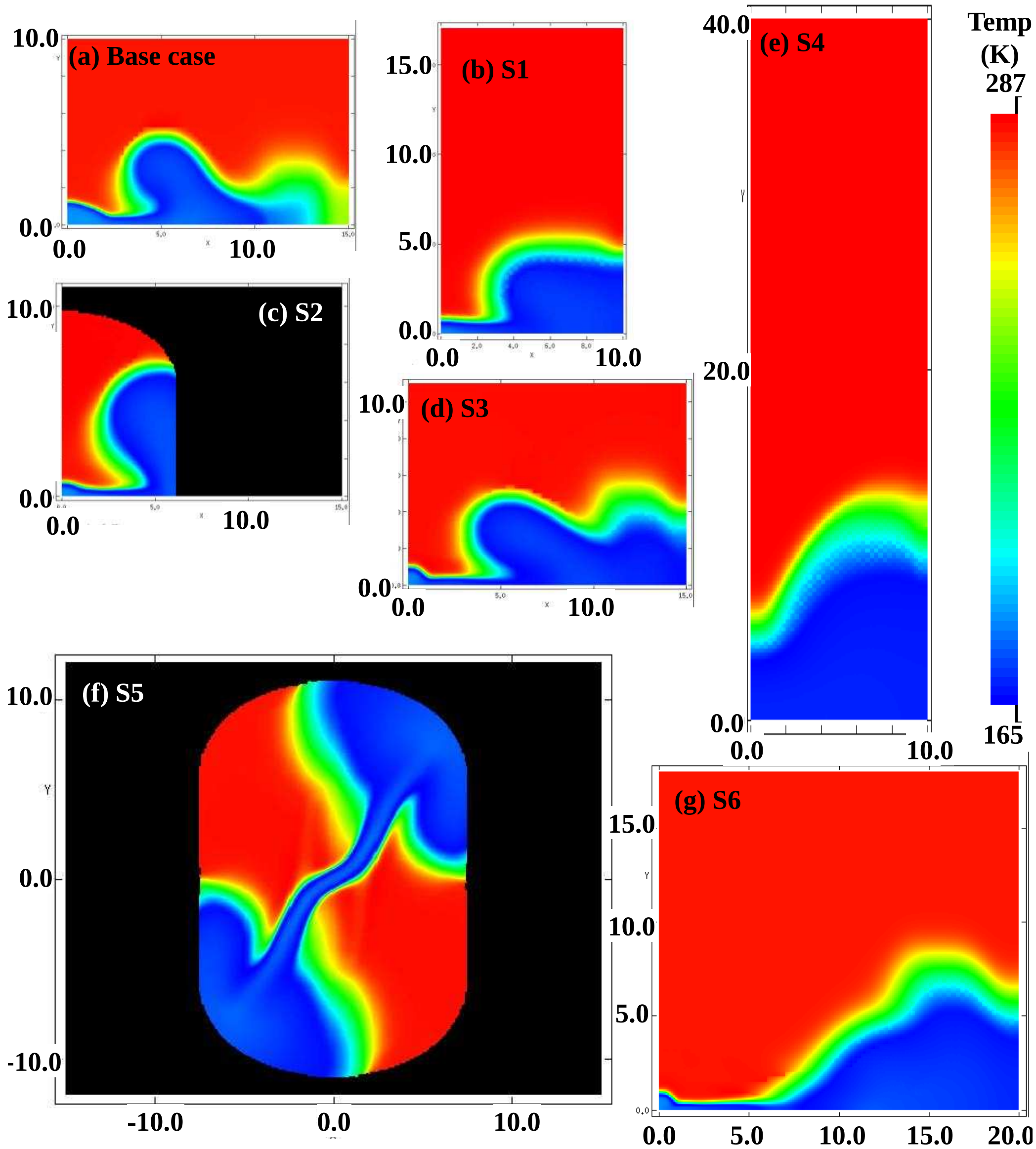

Figure 11: Steady-state flow on horizontal planes above the crater comparing the base case (a) and the six sensitivity studies (b-g) at 250 s after the rupture.

axis at the centre of the crater. At later time the flow was not shifted toward either upstream or downstream inlet pipe. The integrated fluxes are presented in Table 4. At early times, the integrated flow is very similar to that of the equivalent time base case snapshots. At later times, CO_2 fraction and solid fraction linearly decrease, rather than remain constant as in the base case.

5.2. Sensitivity study 2 - a deeper pipeline

In this second sensitivity study (S2), the depth of cover of the pipe is increased from having 1.2 m of soil cover to 2 m of soil cover and the crater depth changed according to Table 2. The motivation for this study is to examine the consequences of a deeper amount of soil cover, as the level of cover is expected to vary along a pipeline as it encounters local geography. A single snapshot at $t = 250$ s was considered for comparison to the base case. The integrated flux on a plane above the crater is presented in Table 5. The effect on the flow out of the crater is minimal. The flow is smooth and has the same structure as the base case snapshot at 250 s, as shown in Figure 11.

5.3. Sensitivity study 3 - a shallower crater

In the third sensitivity study (S3), reducing the crater wall angle is considered - generating a shallower walled crater as detailed in Table 2. The motivation for this study is to examine possible consequences of different soil cover varieties. A single snapshot at $t = 250$ s was simulated for comparison to the base case. The crater wall angle θ was decreased from 75° to 64°. The effect of changing crater wall angle appears only to increase the width of the cloud, allowing for more lateral spreading, as shown in Figure 11, but this is not where the majority of the mass-flux and momentum is located and hence the effect on the plume is minimal. The integrated fluxes are presented in Table 5. The CO_2 fraction and solid fraction are slightly less than the $t = 250$ s results for the base case. Velocity and temperature are very similar to the base case.

5.4. Sensitivity study 4 - a 72 m fracture

In the fourth sensitivity study (S4), modelling of a large crater is performed, detailed in Table 2. The motivation for this study is to examine the consequences of an unarrested pipeline crack creating a 72 m fracture length (L') and associated elongated crater. As this is a considerably different scenario to the base case, all six snapshots of the flow have been simulated in this case. The flow is considerably different, as shown in Figure 11 and in order to establish integrated profiles, slices are higher above the crater than for the base case. The effect is to reduce the CO_2 fraction going upwards in the plume and considerably reduce the solid fraction. Velocities are also lower, as detailed in Table 6. The effect of the extended fracture length is to allow the flow out of each pipe to have a considerable distance to expand and to deflect off the crater base (approximately 36m, rather than 6m in the base case) before meeting in the interaction region in the centre of the crater. Hence much more air is mixed in and CO_2 levels are lower with less solid present. In order to find a plane above the crater that is above this interaction region, it has to be considerably higher than in the base case. On this plane, the plume out of the crater is moving predominantly straight upwards. As the time increases, the CO_2 fraction decreases, the solid fraction decreases and the velocity drops on this plane, as shown in the integrated mass and momentum fluxes in Table 6. The net result is a slower, less concentrated, wider but more collimated flow compared to the base case, as shown in Figure 11.

5.5. Sensitivity study 5 - misaligned pipes

In this sensitivity study (S5), modelling the effect of upstream and downstream pipe inlet misalignment on the flow out of the crater is considered. The misalignment considered, 10° outwards in the horizontal plane, with the 'anchor' point for the pipeline coincident with the crater edge, is an *extreme* case in order to bracket potential real world scenarios. These simulations revealed considerable effects on the flow and all six snapshots of the flow have been simulated in this case. The pipes were misaligned as above, the crater length L was increased to 22 m and the width W to 14.9 m. The structure of the flow is considerably different to the base case and the integrated profiles show larger fractions of CO_2 and larger solid fractions, but comparable velocities and temperatures. Given the nature of the flow, an upwards flow through a plane is of questionable validity here in representing this extreme case. The general crater shape is not changed, although in reality the crater shape will almost certainly be distorted away from the symmetric 'bath-tub' used throughout in this work. The interaction region between the two jets is still in the centre of the crater, although it is now twisted and leads to a upwards flow of CO_2 out of the crater as before, as well as a new flow which consists of the jets from each pipe end partially deflecting off one another, into the opposing crater wall, up the wall and then out of the crater. The shape of the crater strongly affects these new deflected flows. With this crater shape, the flow is deflected upwards out of the crater at the crater wall angle, whilst also carrying momentum in the horizontal plane, resulting in a 'fountain' over opposite edges of the crater, as well as the plume in the middle of the crater, as shown in Figure 11. At early stages, the jets from each pipe and the interaction region dominate, forming a complex plume, but moving predominantly upwards with comparable CO_2 fractions and solid fractions to previous sensitivity studies (as shown in Table 7). The jets do not deflect and there is minimal sideways flow perpendicular and away from the pipeline. By $t = 250$ s into the release, the jets are narrow enough that the major interaction consists of a deflection as the jets pass each other and hence the flow out of the crater is dominated by the crater shape opposite the pipe rupture as the jets hit the opposite walls (see Figure 11. As these flows are complex, the integrated fluxes have been calculated at the crater rim and are shown in Table 7.

5.6. Sensitivity study 6 - sandy soil crater

In this final sensitivity study (S6), the motivation is to study variation in the type of soil cover. Instead of clay, this case considers sandy soil and hence a much wider and longer crater with a shallower wall angle. A single snapshot at $t = 250$ s is presented for comparison to the base case in Figure 11. The crater length L was increased to 33.9 m, the width W to 26.8 m and the crater wall angle θ decreased to $40°$, as detailed in Table 2. The effect on the upwards plume in the centre of the crater is minimal, although the lateral spreading of the plume at ground level is considerably widened by the larger crater and shallower wall angle, as shown in Figure 11. As the depth and fracture length remain the same, there is minimal effect of soil type on the plume going upwards from the centre of the crater. This is the region of the flow carrying the greatest amount of material at the highest velocities. The key effect is as a result of the widening of the crater. The lateral spread of the cloud from the central interaction region is less focussed around the crater as the crater wall angle is considerably far less than previously which means the flow more easily runs up and over the lip of the crater heading perpendicularly away from the pipeline. The velocities in this lateral cloud are very low though. The integrated fluxes presented in Table 5 show that the CO_2 fraction and solid fraction are slightly less than those in the $t = 250$ s snapshot for the base case. Velocity and temperature are very similar to the base case $t = 250$ s snapshot.

6. Discussion

The validation of the pipeline rupture model presented in Part I, and comparisons to experimental data published elsewhere (Woolley et al., 2013; Wareing et al., 2013b, 2014a,b), have shown that in general, this dispersion model can predict the characteristics of high pressure releases of CO_2 from reservoir conditions similar to those under consideration in the CCS industry, including releases directly to air (as in venting operations), punctures and ruptures of below-ground pipelines.

These predictions have required a complex equation of state which accounts not only for accurate behaviour in the gas phase, but also, because of the temperature range from the release point into the far-field, for accurate behaviour in the liquid and solid phases and the transition to the solid phase.

The method used here has modelled steady-state snapshots at a number of points in the decompression of the pipeline. Based on short dynamic and thermal relaxation times, the short flow-crossing time of the near-field and the slow variation of the ruptured pipe inlet conditions, the pipeline goes through a sequence of steady-states during the decompression. The choice of only examining a number of these, limited by the high computational expenses of accurately modelling the near-field thermodynamics and ensuring resolution of the near-field shock structures is therefore justified. However, it should be noted that by taking such snapshots of the flow at instants in time, the precludes any effect on the steady state snapshot in question of the earlier evolution of the flow, theoretically minimal as it may be. Future software and hardware developments may allow the investigation of a complete depressurisation of a full-scale pipeline, with the necessary accuracy and resolve any questions over the transient nature of the dispersion flow and the assumption that it has no 'memory'.

Water vapour in the atmosphere will also affect the flow, but have limited bearing on the true near-field. Predictions indicate that a free jet is entirely CO_2 until approximately 40 release diameters downstream from the release point. Any water vapour in the air cannot affect the core whilst it is 100% CO_2, so it is unlikely to have an effect on the true near-field around the Mach shock as that is always within 10 diameters of the release point. Given the likely size of craters formed in pipeline ruptures, it is unlikely to strongly affect the flow *in the crater* of a full-scale rupture. Once air does begin to mix into the core, water ice will form in the low temperature environment and since water has a latent heat of fusion greater than that of CO_2, it will be an energy sink and the CO_2 jet itself will not be as cold as a consequence.

Also, the jet formed will be more buoyant. Water droplets condensed by the cold jet will also define the visual extent of the jet. This is true throughout the jet, but requires air to mix into the jet, which initially in the near-field happens at very low levels. Following the interaction region in the crater, water vapour condensing when the temperature drops below the dew point will visually define the outer extent of the jet.

Re-entrainment of CO_2 back into a crater has been considered in two ways. Taking far-field predictions, a mixture containing 15% CO_2 and 85% air by mass was allowed to flow into the simulation domain in previous puncture studies (Wareing et al., 2014b), at ambient temperatures and pressures as predicted by the far-field simulation. This appeared to have no effect on the crater outflow. In the second examination, a simplified two dimensional simulation of a stalling plume was considered, as the full simulation is not possible with a near-field model alone. The results have shown that plume height is affected - it drops by one third as the cold cloud is re-entrained into the flow. Further full far-field simulations modelling the crater and employing near-field predictions, just past the Mach shock but before the interaction region in the crater, as input could be used to explore this issue further. It is possible to conclude from the tests conducted that in these scenarios, re-entrainment of ambient temperature, low concentration dispersing CO_2 into the crater has little effect on a crater outflow, but re-entrainment of a stalling plume, containing high concentration, cold CO_2 does have an effect on the plume, leading to a lower stalling height and different dispersion properties.

A homogeneous equilibrium model has also been used throughout the simulations presented here. In the case of ruptures, this is entirely applicable, as discussed in detail elsewhere (Wareing et al., 2013b), since the particles will be in equilibrium with the flow and follow the flow streamlines.

The choice of turbulence model has a bearing on the predictions. These simulations have employed the $k - \epsilon$ turbulence model with a compressibility correction required by the decompression of the highly-underexpanded pipeline flow. We have shown previously that this model is capable of modelling free releases into air (Wareing et al., 2014a). To ensure compatibility within the COOLTRANS research programme, we continued to employ this model for the below-ground releases, with good results for punctures compared to experimental data (Wareing et al., 2014b). However, a Reynolds-stress turbulence model would be more appropriate for these situations. Even with such a second-moment turbulence closure, it is not possible to capture the true transient turbulent nature of these releases with a RANS model, as the model is *time-averaged* predicting a time-averaged structure. Large eddy simulation could be advantageously employed, but questions then have to be answered as to how this would link with pipe-flow and near-field models and feed into the RANS methods common in industry.

Further simulations of complex particle interactions will provide more clarity, especially when considered in combination with far-field dispersion calculations to estimate rain-out of solid CO_2, as the heaviest agglomerates are probably formed in the interaction region in the middle of the crater. Given the assumptions above about where particles deposit, these should be considered upper limit estimates based on the method and analysis applied. However, it is difficult to apply these general assumptions. Given the behaviour in the case of releases from pipeline punctures (Wareing et al., 2014b), the simulations indicate that deposition could alter the profile of the crater in such a way as to provide a 'smooth' flow path and inhibit further deposition. It would be fair to say then that the 1% estimate is a 'peak' rate of deposition and that once significant accumulation of solid occurs in the crater, the flow may adapt to reduce this rate, thereby reducing the estimates of total deposition made above considerably further.

In previous work (Wareing et al., 2014b), we have estimated particle deposition rates for punctures of buried pipelines. Predicted particle behaviour and deposition was seen in the experiments. There exists no evidence to support or contradict the level of particle deposition estimated here - horizontal venting experiments in CO2PIPETRANS have shown piles of solid CO_2 under impact plates and deposition has been seen in both the puncture experiments mentioned above and in the quarter scale rupture experiment used for validation of this method in Part I, so we have reasonable confidence in saying there will certainly be some particle deposition. Scaling up puncture and quarter scale rupture experiments indicate it may be a considerable amount, not entirely different to the amounts calculated above. Particle collision and agglomeration, not included, may also be significant in these rupture flows.

Whatever the amount of CO_2 in or around the crater, it should be separately considered for further risk analysis as a secondary source of a dispersing gas cloud after a rupture event, separate to the dispersion of the gas cloud as a result of the rupture itself. It should also be noted that these are very simple estimates that can be changed considerably by small changes in assumptions, e.g. assuming 0.5% deposition and the quantity deposited drops by a factor two. Without further refinement, and possibly testing of different ways of introducing particles and capturing their behaviour, they should be used with extreme caution in any future work. Further experimental data is required to refine these predictions.

The sensitivity study of the base case has shown how different crater parameters affect the flow out of the crater. It is reasonable to say that the greatest effect comes from mis-aligning the pipes in Sensitivity study 5, although the case considered is an extreme one and further studies would be required to investigate the impact of, and corresponding changes to, the crater geometry as a results of jet impingement on the crater walls. Otherwise, a much increased fracture length (on the order of 72m) also has a large effect on the flow structure, but not that much of an effect on the integrated profiles. Changing the pipe depth, pipe section length, crater wall angle or soil type have effects on the flow structure that can be understood in terms of the parameter change, but are relatively minimal, especially when considering the integrated fluxes. It should be safe to assume that in all cases, except the pipe mis-alignment case, a maximum of 1% of the particles released end up in the base of the crater. The above results could also be interpreted to mean that during balanced flow, all particles flow out of the crater, but this would seem to be the other extreme of the scale and would ignore any possibility of particle collisions in the interaction region that would drive particles into the crater base. In the case of mis-aligned pipe inlets, considerably more solid CO_2 may stay in the crater as the flows are deflected into the crater walls, where particles will embed. However, the bath-tub crater shape used is in fact unlikely to be the shape of the crater in such a mis-aligned release and hence this result should again be used with caution. Further numerical and experimental testing is required to elucidate this issue.

7. Conclusions

This article has presented the application of a novel method for simulating sonic high pressure releases of dense-phase CO_2 to the realistic scenario of a rupture of a buried pipeline. The pipeline rupture proceeds through a sequence of steady-states, or snapshots. Due to computational time constraints, only a number of these snapshots have been modelled. Integrated fluxes have been produced for the flow out of the crater, providing significantly novel initial conditions beyond the shock-containing thermodynamically-complex near-field. Future far-field dispersion simulations can now employ these integrated fluxes as source conditions and avoid the need to accurately model the near-field conditions.

A set of six sensitivity studies has also been presented, examining the effect of varying crater parameters on the flow out of the crater. Integrated fluxes are also presented for each of these sensitivity studies. All these near-field predictions have required a three-phase accurate equation of state, that also accounts for the latent heat of fusion.

Extrapolations of the integrated fluxes to the full transient decompression will now also be considered. Further experimental data at both laboratory-scale and larger scales is required to further validate the model and shed light on the behaviour of solid CO_2 in and around the crater, although we have used Lagrangian particle tracking methods and appropriate conditions derived from laboratory-scale experiments to estimate particle deposition rates into the crater in this work.

Acknowledgements

During the undertaking of this work, CJW was supported by the COOLTRANS research programme (Cooper, 2012), part of the Don Valley CCS Project, and CJW and MF would like to thank National Grid and the European Union's European Energy Programme for Recovery for their support of the work described herein. We acknowledge the provision of information regarding pipe inlet conditions from UCL (V. Sundara, S. Brown and H. Mahgerefteh) and useful critiques from anonymous reviewers which improved the original manuscript. The calculations for this paper were performed on the DiRAC Facility jointly funded by STFC, the Large Facilities Capital Fund of BIS and the University of Leeds and the N8 HPC facility jointly funded by the N8 consortium and EPSRC (Grant No.EP/K000225/1). Both are hosted and enabled through the ARC HPC resources and support team at the University of Leeds (A. Real, M. Dixon, M. Wallis, M. Callaghan & J. Leng).

References

Allason, D., Armstrong, K., Cleaver, P., Halford, A., Barnett, J., 2012. Experimental studies of the behaviour of pressurised release of carbon dioxide. In: IChemE Symposium Series No. 158, IChemE. pp. 142–152.

Brown, S., Martynov, S., Mahgerefteh, M., Proust, C., 2013. A homogeneous equilibrium relaxation flow model for the full bore rupture of dense phase CO_2 pipelines. Int. J. Greenhouse Gas Control 17, 349–356.

Cooper, R., 2012. National Grid's COOLTRANS research programme. Journal of Pipeline Engineering 11, 155–172.

Cooper, R., Barnett, J., 2014. Pipelines for transporting CO_2 in the UK. Energy Procedia 63, 2412–2431.

Cumber, P.S., Fairweather, M., Falle, S.A.E.G., Giddings, J.R., 1994. Predictions of the structure of turbulent, moderately underexpanded jets. Journal of Fluids Engineering 116, 707–713.

Cumber, P.S., Fairweather, M., Falle, S.A.E.G., Giddings, J.R., 1995. Predictions of the structure of turbulent, highly underexpanded jets. Journal of Fluids Engineering 117, 599–604.

Falle, S.A.E.G., 1991. Self-similar jets. Monthly Notices of the Royal Astronomical Society 250, 581–596.

Falle, S.A.E.G., 2005. AMR applied to non-linear elastodynamics, in: Plewa, T., Linde, T., Weirs, V.G. (Eds.), Proceedings of the Chicago Workshop on Adaptive Mesh Refinement Methods, Springer Lecture Notes in Computational Science and Engineering v.41, Springer, New York U.S.A.. pp. 235–253.

Godunov, S.K., 1959. A difference scheme for numerical computation of discontinuous solutions of equations of fluid dynamics. Matematicheskii Sbornik 47, 271–306.

Harten, A., Lax, P.D., van Leer, B., 1983. On upstream differencing and Godunov-type schemes for hyperbolic conservation laws. SIAM Review 25, 35–61.

Peng, D.Y., Robinson, D.B., 1976. A new two-constant equation of state. Industrial and Engineering Chemistry: Fundamentals 15, 59–64.

Sarkar, S., Erlebacher, G., Hussaini, M.Y., Kreiss, H.O., 1991. The analysis and modelling of dilatational terms in compressible turbulence. Journal of Fluid Mechanics 227, 473–493.

Span, R., Wagner, W., 1996. A new equation of state for carbon dioxide covering the fluid region from the triple-point temperature to 1100 K at pressures up to 800 MPa. Journal of Physical and Chemical Reference Data 25, 1509–1596.

van Leer, B., 1977. Towards the ultimate conservative difference scheme. IV. A new approach to numerical convection. Journal of Computational Physics 23, 276–299.

Wareing, C., Woolley, R.M., Fairweather, M., Falle, S.A.E.G., 2013a. A composite equation of state for the modelling of sonic carbon dixoide jets in carbon capture and storage scenarios. AIChE Journal 59, 3928–3942.

Wareing, C., Fairweather, M., Peakall, J., Keevil, G., Falle, S.A.E.G., Woolley, R.M., 2013b. Numerical modelling of particle-laden sonic CO_2 jets with experimental validation, in: Zeidan, D. (Ed.), AIP Conference Proceedings of the 11th International Conference of Numerical Analysis and Applied Mathematics, AIP Publishing. pp. 98–102.

Wareing, C., Fairweather, M., Falle, S.A.E.G., Woolley, R.M., 2014a. Validation of a model of gas and dense phase CO_2 jet releases for carbon capture and storage application. Int. J. Greenhouse Gas Control 20, 254-271.

Wareing, C., Fairweather, M., Falle, S.A.E.G., Woolley, R.M., 2014b. Modelling punctures of buried high-pressure dense phase CO_2 pipelines in CCS applications. Int. J. Greenhouse Gas Control 29, 231-247.

Wareing, C., Fairweather, M., Falle, S.A.E.G., Woolley, R.M., 2015a. Modelling ruptures of buried high-pressure dense phase CO_2 pipelines in carbon capture and storage applications - Part I. Validation. Int. J. Greenhouse Gas Control doi:10.1016/j.ijggc.2015.01.020,

Wareing, C., Woolley, R.M., Fairweather, M., Peakall, J., Falle, S.A.E.G., 2015b. Numerical modelling of turbulent particle-laden sonic CO_2 jets with experimental validation. Procedia Engineering 102, 1621-1629.

Woolley, R.M., Fairweather, M., Wareing, C.J., Falle, S.A.E.G., Proust, C., Hebrard, J., Jamois, D., 2013. Experimental measurement and Reynolds-averaged Navier-Stokes modelling of the near-field structure of multi-phase CO_2 jet releases. Int. J. Greenhouse Gas Control 18, 139–149.

Woolley, R.M., Fairweather, M., Wareing, C.J., Proust, C., Hebrard, J., Jamois, D., Narasimhamurthy, V.D., Storvik, I.E., Skjold, T., Falle, S.A.E.G., Brown, S., Mahgerefteh, H., Martynov, S., Gant, S., Tsangaris,D.M., Economou, I.G., Boulougouris, G.C., Diamantonis, N.I.., 2014. An integrated, multi-scale modelling approach for the simulation of multiphase dispersion from accidental CO_2 pipeline releases in realistic terrain. Int. J. Greenhouse Gas Control 27, 221–238.

Notation

Roman letters:

a	model parameter
b	model parameter
c	adiabatic sound speed
C	specific heat
d	non-dimensional nozzle diameter
e	total energy per unit volume
F	Helmholtz free energy
k	turbulence kinetic energy
m	mass
p	pressure
r	non-dimensional radial location
R	universal gas constant
t	time
S	entropy
T	temperature
u	magnitude of velocity
U	internal energy per unit mass
v	molar volume
w	molecular weight
z	non-dimensional axial location

Greek letters:

α	condensed phase fraction
β	total mass fraction of CO_2
δ	Peng-Robinson equation of state parameter
ϵ	dissipation rate of k
γ	ratio of specific heats
μ	molecular viscosity
ρ	density
τ	relaxation time
ω	acentric factor of the species

Subscripts:

0	reference state
a	air
c	condensed phase
crit	critical point
g	gas
i	initial
mix	mixture
s	saturation
trip	triple point
v	vapour

Table 1: Initial upstream and downstream pipe outflow conditions for the rupture cases (Mahgerefteh, private communication).

Time s	Stream direction	Pressure 10^6 Pa	Temp. K	CO_2 %	Liquid %	Velocity $m\,s^{-1}$	Mass-flow $kg\,s^{-1}$
30	Up	1.971	253.3	100.0	69.0	98.19	3773
30	Down	1.971	253.3	100.0	69.0	98.19	3773
100	Up	1.403	242.8	100.0	64.0	108.5	2661
100	Down	1.403	242.8	100.0	64.0	108.5	2661
250	Up	1.060	234.8	100.0	61.0	114.0	1992
250	Down	1.060	234.8	100.0	61.0	114.0	1992
600	Up	8.12	227.7	100.0	58.0	119.4	1506
600	Down	7.55	225.8	100.0	58.0	120.1	1402
1000	Up	7.14	224.4	100.0	57.0	121.5	1334
1000	Down	5.98	220.1	100.0	56.0	123.3	1118
1150	Up	6.42	221.8	100.0	57.0	122.2	1205
1150	Down	5.16	216.6	100.0	55.0	124.2	971.0

Table 2: Crater parameters for the base rupture case and the range of sensitivity studies considered.

Case #	Fracture Length L'(m)	Crater Description	Length L(m)	Width W(m)	Depth D(m)	Wall angle $\theta°$
Base	12	Clay soil, 1.2m depth	18.5	11.4	3.2	75
S1	24	Longer pipeline fracture	30.5	11.4	3.2	75
S2	12	Pipe top at 2m depth	19.4	12.3	4.0	75
S3	12	Shallower wall angle	18.5	11.4	3.2	64
S4	72	Longer fracture	78.5	11.4	3.2	75
S5	12	Pipes misaligned by 10°	22.0	14.9	3.2	75
S6	12	Sandy soil crater	33.9	26.8	3.2	40

Table 3: Snapshot integrated fluxes above the crater in the base rupture case.

Time (s)	30	100	250	600	1000	1150
Plane at:	2m	2m	1m	1m	1m	1m
Mass-flow	($kg\,s^{-1}$)					
Total up	12700	9830	6990	5290	4330	4080
Total down	1030	1710	1960	1190	1150	1360
CO_2 up	7550	5810	4320	2990	2600	2370
CO_2 down	15.8	43.8	48.9	134	200	145
Solid up	1440	1010	801	455	443	502
Solid down	0.020	0.064	0.006	0.197	1.54	0.404
Momentum	($kg\,m\,s^{-2}$)					
Total up	914000	637000	415000	233000	171000	155000
Total down	4388	11900	18500	19500	9350	8740
CO_2 up	600000	444000	290000	142000	107000	94400
CO_2 down	82.4	239	243	1460	1210	972
Solid up	126000	93200	62000	25600	20000	21200
Solid down	0.111	0.307	0.004	2.190	8.018	2.386
Velocity	($m\,s^{-1}$)					
Up	72.1	64.9	59.3	44.1	39.5	37.9
CO_2 up	79.5	76.4	67.1	47.7	41.3	39.8
Solid up	87.1	91.9	77.4	56.3	45.2	42.3
Peak	188	129	164	150	141	134
Temp.	192 K	188 K	189 K	186 K	188 K	187 K

Table 4: Snapshot integrated fluxes above the crater for Sensitivity Study 1.

Time (s)	30	100	250	600	1000	1150
Plane height:	2m	2m	2m	1m	1m	1m
Mass-flow	($kg\,s^{-1}$)					
Total up	11900	9230	7350	5890	5510	5050
Total down	3440	3080	2870	2820	2840	2610
CO_2 up	7540	5280	3840	2960	2520	2340
CO_2 down	78.8	49.3	35.1	53.4	33.5	57.9
Solid up	1440	859	518	386	292	323
Solid down	9.37	2.80	0.870	1.09	0.133	0.208
Momentum	($kg\,m\,s^{-2}$)					
Total up	873000	651000	457000	333000	286000	226000
Total down	34600	28900	24700	26700	32300	25600
CO_2 up	597000	410000	268000	192000	154000	117000
CO_2 down	290	228	183	291	201	597
Solid up	125000	76900	44600	31300	22700	20000
Solid down	16.3	2.52	0.585	1.32	0.226	0.725
Velocity	($m\,s^{-1}$)					
Upwards	73.6	70.6	62.2	56.6	52.0	44.7
CO_2 up	79.2	77.7	69.7	64.8	60.9	50.2
Solid up	86.5	89.5	86.1	81.3	77.7	61.9
Peak	169	156	149	155	153	142
Temp. (K)	188	188	188	188	191	188

Table 5: Integrated fluxes for the snapshots at $t = 250$ s Sensitivity Studies 2, 3 and 6.

Sensitivity study	S2	S3	S3
Plane height (m)	0	2	1
Mass-flow ($\mathrm{kg\,s^{-1}}$)			
Total up	6530	7170	7090
Total down	2500	2080	3090
CO_2 up	4020	3910	3830
CO_2 down	144	231	78.7
Solid up	735	578	584
Solid down	0.380	6.76	6.38
Momentum ($\mathrm{kg\,m\,s^{-2}}$)			
Total up	482000	373000	362000
Total down	9320	18800	18100
CO_2 up	324000	241000	240000
CO_2 down	1470	1580	108
Solid up	66500	45700	48600
Solid down	2.13	53.6	10.7
Velocity ($\mathrm{m\,s^{-1}}$)			
Inferred up	73.8	52.1	51.0
Inferred CO_2 up	80.7	61.5	62.7
Inferred solid up	90.5	79.1	83.3
Flow-weighted temp. (K)	188	188	190

Table 6: Snapshot integrated fluxes above the crater for Sensitivity Study 4.

Time (s)	30	100	250	600	1000	1150
Plane height:	6m	5.5m	6m	6m	5m	6m
Mass-flow	($kg\,s^{-1}$)					
Total up	14800	11700	9540	7700	6850	6500
Total down	4150	4180	3550	2830	2860	2680
CO_2 up	7540	5320	3980	2910	2440	2180
CO_2 down	3.79	5.52	1.11	1.06	5.09	0.85
Solid up	934	461	238	81.9	30.1	113
Solid down	0.0	0.0	0.0	0.0	0.0	0.0
Momentum	($kg\,m\,s^{-2}$)					
Total up	391000	267000	164000	93800	72700	61700
Total down	26200	26400	18600	12600	12800	11800
CO_2 up	209000	128000	70800	36000	26200	20800
CO_2 down	16.3	20.8	3.0	2.6	14.6	2.2
Solid up	7070	12400	4600	1010	307	1060
Solid down	0.0	0.0	0.0	0.0	0.0	0.0
Velocity	($m\,s^{-1}$)					
Inferred up	26.3	22.9	17.2	12.2	10.6	9.5
Inferred CO_2 up	27.7	24.0	17.8	12.4	10.7	9.6
Inferred solid up	7.6	26.9	19.3	12.3	10.2	9.4
Peak	50.6	42.0	29.8	23.9	26.6	21.6
Temp. (K)	186	186	186	188	190	187

Table 7: Snapshot integrated fluxes above the crater for Sensitivity Study 5.

Time (s)	30	100	250	600	1000	1150
Plane height:	0m	0m	0m	0m	0m	0m
Mass-flow	($kg\,s^{-1}$)					
Total up	11000	7820	6360	4970	4290	3580
Total down	4230	2490	2350	1870	1650	1480
CO_2 up	7720	5400	4030	2980	2510	2120
CO_2 down	570	53.2	150	125	152	166
Solid up	1730	1160	755	510	408	418
Solid down	1.73	0.06	0.22	0.39	0.86	8.88
Momentum	($kg\,m\,s^{-2}$)					
Total up	496000	369000	276000	162000	119000	85100
Total down	134000	30200	30700	19000	16400	12600
CO_2 up	378000	273000	185000	102000	72800	53400
CO_2 down	17800	433	2030	1270	1860	1670
Solid up	89600	62200	38000	18900	12800	11200
Solid down	28.3	0.41	2.19	1.76	5.20	76.7
Velocity	($m\,s^{-1}$)					
Upwards	45.2	47.2	43.4	32.6	27.6	23.7
CO_2 up	49.0	50.6	45.9	34.2	29.0	25.2
Solid up	51.9	53.7	50.3	37.1	31.3	26.7
Peak	245	207	162	140	109	83.6
Temp. (K)	191	190	188	187	186	186